

Interactive effects of the El Niño-Southern Oscillation and Indian Ocean Dipole on the tropical net ecosystem productivity

Ran Yan ^a, Jun Wang ^{a,b,*}, Weimin Ju ^a, Daniel S. Goll ^c, Atul K. Jain ^d, Stephen Sitch ^e, Hanqin Tian ^f, Poulter Benjamin ^g, Fei Jiang ^a, Hengmao Wang ^a

^a *Frontiers Science Center for Critical Earth Material Cycling, International Institute for Earth System Science, Nanjing University, Nanjing 210023, China*

^b *Key Laboratory of Meteorological Disaster (KLME), Ministry of Education & Collaborative Innovation Center on Forecast and Evaluation of Meteorological Disasters (CIC-FEMD), Nanjing University of Information Science & Technology, Nanjing 210044, China*

^c *Laboratoire des Sciences du Climat et de l'Environnement, LSCE/IPSL, CEA-CNRS-UVSQ, Université Paris-Saclay, F-91198, Gif-Sur-Yvette, France*

^d *Department of Atmospheric Sciences, University of Illinois, Urbana, IL, 61801 USA*

^e *Department of Geography, Faculty of Environment, Science and Economy, University of Exeter, UK*

^f *Schiller Institute for Integrated Science and Society, Department of Earth and Environmental Sciences, Boston College, Chestnut Hill, MA 02467, USA*

^g *NASA Goddard Space Flight Center, Biospheric Sciences Laboratory, Greenbelt, MD, USA*



ARTICLE INFO

Keywords:

Net ecosystem productivity
El Niño-Southern Oscillation
Indian Ocean Dipole
Interactive effects
Terrestrial biosphere models

ABSTRACT

El Niño-Southern Oscillation (ENSO) and Indian Ocean Dipole (IOD) can exert abiotic stresses on biota to influence regional terrestrial carbon cycling. Here, we investigated their interactive effects on tropical net ecosystem productivity (NEP) when ENSO and IOD simultaneously occur (mainly El Niño & positive IOD [pIOD] and La Niña & negative IOD [nIOD]), based on TRENDYv9 multi-model simulations. Results suggest that NEP anomalies were dominated by IOD over South America near 20°S and Africa south of the Equator, but by ENSO over India and northern South America, and controlled by their amplifying effects over eastern Africa, the Indo-China peninsula, and most of Australia during September-October-November (SON). In the following December-January-February (DJF), IOD legacy effects generally enhanced ENSO-induced NEP anomalies over most of South America, eastern and southern Africa, and Australia. During March-April-May (MAM), the influence of IOD gradually disappeared. Our analysis revealed the dominant role of gross primary productivity (GPP) in these NEP anomalies. We further found asymmetric effects of soil moisture and temperature on NEP anomalies, showing higher correlation coefficients with soil moisture in El Niño & pIOD, but basically with temperature in La Niña & nIOD. Additionally, considering the simultaneous extreme of pIOD and El Niño activity in 1997/98, we calculated their seasonal individual contributions to NEP anomalies. We found that the pIOD event had the greatest influence in SON. During SON in 1997, individual contributions of pIOD and El Niño to NEP caused a land carbon source of -0.34 ± 0.15 and $-0.35 \pm 0.32 \text{ PgC yr}^{-1}$ over South America, a carbon sink and source of 0.5 ± 0.19 and $-0.54 \pm 0.14 \text{ PgC yr}^{-1}$ over Africa, and source of -0.08 ± 0.25 and $-0.42 \pm 0.37 \text{ PgC yr}^{-1}$ over Asia-Pacific, respectively. Understanding interactive effects of IOD and ENSO on regional carbon cycling is crucial due to the more frequent extreme IOD and ENSO events under future climate warming.

1. Introduction

Large-scale oceanic and atmospheric oscillations can greatly affect terrestrial ecosystems and their carbon fluxes (Bacastow, 1976; Bastos et al., 2016; Bousquet et al., 2000; Wang et al., 2021). The El Niño-Southern Oscillation (ENSO), a leading mode of Earth's interannual climate variability, is characterized by sea surface temperature (SST) and surface pressure anomalies across the tropical Pacific Ocean

(Trenberth et al., 2007). ENSO events can alter temperature, precipitation, and solar radiation over land, thereby affecting terrestrial carbon cycling (Bousquet et al., 2000; Kim et al., 2017; Piao et al., 2020; Wang et al., 2016, 2018a; Zeng et al., 2005). Terrestrial ecosystems, especially over the tropics, tend to release carbon into the atmosphere during El Niño episodes while removing carbon from the atmosphere during La Niña episodes (Liu et al., 2017; Wang et al., 2018b; Zeng et al., 2005). This contributes to the observed interannual variation in the

* Corresponding author.

E-mail address: wangjun@nju.edu.cn (J. Wang).

atmospheric CO₂ growth rate (CGR) (Bousquet et al., 2000; Peylin et al., 2013). Many studies have indicated that during El Niño drier and warmer conditions throughout the tropics lead to increased tree mortality and decreased aboveground carbon stocks (Phillips et al., 2009), inhibited photosynthesis (Bastos et al., 2018; Luo et al., 2018; Wang et al., 2018a; Yang et al., 2018), increased soil respiration (Zeng et al., 2005), and increased wildfires (Bowman et al., 2009; van der Werf et al., 2004). Nevertheless, there is a debate on the dominant climate factor driving the interannual variability of the atmospheric CGR or net land-atmosphere carbon flux among the temperature, precipitation (or soil moisture), and vapor pressure deficit (VPD) (He et al., 2022; Humphrey et al., 2021, 2018; Jung et al., 2017; Wang et al., 2016, 2013).

More recently, the Indian Ocean Dipole (IOD), another coupled ocean-atmosphere mode, received some attention in its role in the regional carbon cycling (Wang et al., 2021; Williams and Hanan, 2011). The IOD is characterized by the positive (negative) phase of the warm (cold) SST over the western tropical Indian Ocean (WTIO) and cool (warm) SST in the southeastern tropical Indian ocean (SETIO) during boreal summer and fall (Saji et al., 1999). Although IOD has been recognized for about two decades (Saji et al., 1999), existing studies focused mainly on its impact on the climate, especially the Indian Ocean (IO) rim countries (Ashok et al., 2004; Cai et al., 2011; Saji and Yamagata, 2003). In a positive IOD (pIOD) event, a warm pole over the WTIO tends to cause heavy rainfall or flooding in Eastern Africa and India associated with active convection. On the other hand, cold SSTs over the SETIO can cause hot droughts in Australia, Indonesia, and the Indo-China Peninsula (Kim et al., 2019; Preethi et al., 2015). In terms of terrestrial carbon cycling, Cai et al. (2009) suggested that the pIOD event increased temperate forest fire occurrence over southeastern Australia, and associated release of CO₂ to the atmosphere (van der Velde et al., 2021; Wang et al., 2020). Wang et al. (2021) analyzed the effect of pIOD on historical and future gross primary productivity (GPP) over the IO rim countries. They revealed that partial correlation coefficients between IOD and GPP, controlling for the effect of ENSO, are significantly positive in most of Africa and India, but significantly negative in southern China, the Indo-China Peninsula, the maritime continent, and Australia, which were mainly related to precipitation variations.

Although IOD events were suggested as a coupled ocean-atmosphere interaction independent from that of ENSO (Saji et al., 1999), historical IOD events tend to occur with ENSO in addition to the single events (the occurrence of IOD events in the absence of an ENSO event) (Ham et al., 2016; Yang et al., 2015). A compound event (the occurrence of IOD simultaneously with ENSO events) can increase constructively the impacts of the ENSO event, even exceed the climate impact of extremely strong sole El Niño events (Hameed et al., 2018). A previous study (Williams and Hanan, 2011) investigated the interactive effects of ENSO and IOD on African GPP, based on the Simple Biosphere model, Version 3 (SiB3) with the offline mode. They found that IOD could induce large departures of GPP across much of Africa, which can suppress or even reverse ENSO signals in GPP anomalies. However, the interactive effect of ENSO and IOD events on the net land-atmosphere carbon flux remains unclear.

This study aims to give new insights into the interannual variability of tropical terrestrial carbon cycling. Specifically, we will investigate the interactive effect of ENSO and IOD events during periods of simultaneous ENSO and IOD activity on the tropical net ecosystem productivity (NEP, the positive value denotes a land carbon sink) and compared it to the impacts of individual ENSO or IOD events based on the multi-model simulations from the “Trends and drivers of the regional scale sources and sinks of carbon dioxide” (TRENDY) project. Composite analysis will be adopted to qualitatively analyze the roles of ENSO and IOD in NEP anomalies over different tropical regions in different seasons during periods of simultaneous IOD and ENSO activity. In addition, due to the high impact of extreme events, we will focus on the compound event in

1997/98, in which simultaneous extreme El Niño and pIOD occurred, to quantitatively show their individual contributions to NEP anomalies over the three tropical sub-continents.

2. Datasets and methods

2.1. TRENDYv9 multi-model simulations

We used outputs from the state-of-the-art terrestrial biosphere models (TBMs) under the auspices of the TRENDY Project (Sitch et al., 2015). There are three main experimental protocols in the TRENDY project, including S1 with dynamic CO₂ only, S2 with dynamic CO₂ and climate, and S3 with dynamic CO₂, climate, and land-use (Sitch et al., 2015). And the S3 run in TRENDYv9 was adopted in this study.

We screened out some models with opposite spatial patterns of NEP from the multi-model ensemble mean result and satellite-derived pattern revealed by the previous study (Wang et al., 2021). Eleven TBMs were retained here, including CLASSIC (Melton et al., 2020), DLEM (Tian et al., 2015), ISAM (Jain et al., 2013), ISBA-CTRP (Delire et al., 2020), LPJ (Poulter et al., 2011), LPX-Bern (Lienert and Joos, 2018), OCN (Zaehle et al., 2010), ORCHIDEE (Krinner et al., 2005), ORCHIDEE-CNP (Goll et al., 2017), ORCHIDEEv3 (Vuichard et al., 2019), and SDGVM (Walker et al., 2017) (Table 1). We analyzed four variables, gross primary productivity (GPP), total ecosystem respiration (TER, sum of autotrophic and heterotrophic respiration), net ecosystem production (NEP = GPP – TER), and root zone soil moisture (denoted as ‘MRSO’ in outputs). Considering the different horizontal resolutions among different TBMs, we first interpolated all the variables consistently to a 1° × 1° spatial resolution by using the first-order conservative remapping scheme (Jones, 1999) in Climate Data Operators (CDO) with the formula as below:

$$\bar{F}_k = \frac{1}{A_k} \iint f dA \quad (1)$$

where \bar{F}_k represents the area-averaged destination flux, A_k is the area of cell k, and f is the original flux in an old grid which can have an overlapping area with the destination grid.

Table 1
Terrestrial biosphere models (TBMs) used in this study.

Models	Spatial resolution	GPP	TER ^a	NEP ^b	MRSO	References
CLASSIC	T42	✓	✓	✓	✓	Melton et al. (2020)
DLEM	0.5° × 0.5°	✓	✓	✓		Tian et al. (2015)
ISAM	0.5° × 0.5°	✓	✓	✓	✓	Jain et al. (2013)
ISBA-CTRP	1° × 1°	✓	✓	✓	✓	Delire et al. (2020)
LPJ	0.5° × 0.5°	✓	✓	✓		Poulter et al. (2011)
LPX-Bern	0.5° × 0.5°	✓	✓	✓	✓	Lienert and Joos (2018)
OCN	1° × 1°	✓	✓	✓	✓	Zaehle and Friend (2010)
ORCHIDEE	0.5° × 0.5°	✓	✓	✓	✓	Krinner et al. (2005)
ORCHIDEE-CNP	2° × 2°	✓	✓	✓	✓	Goll et al. (2017)
ORCHIDEEv3	0.5° × 0.5°	✓	✓	✓	✓	Vuichard et al. (2019)
SDGVM	1° × 1°	✓	✓	✓	✓	Walker et al. (2017)

^a TER denotes the total ecosystem respiration, calculated by the sum of autotrophic and heterotrophic respiration ($R_a + R_h$).

^b NEP denotes the net ecosystem productivity. Some are provided directly from the model, and some are computed from GPP minus TER (GPP-TER).

2.2. Surface air temperature and sea surface temperature

We used surface air temperature from the gridded Climatic Research Unit (CRU) Time-series (TS) data version 4.05 (Harris et al., 2020). This monthly temperature dataset spans the period from 1901 to 2020 with a $0.5^\circ \times 0.5^\circ$ horizontal resolution. For consistency with TRENDY datasets, we resampled the temperature data to $1^\circ \times 1^\circ$ using the bilinear method.

The sea surface temperature (SST) dataset came from the NOAA's Extended Reconstructed Sea Surface Temperature version 5 (ERSSTv5) (Huang et al., 2017). It was produced at a $2^\circ \times 2^\circ$ grid with spatial completeness enhanced through statistical methods. This monthly SST dataset begins in January 1854, continues to the present, and includes anomalies computed with respect to a 1971–2000 monthly climatology.

2.3. Calculation of anomalies

To calculate anomalies, we first removed the long-term climatology to eliminate the seasonal cycle, and detrended the resulting data using linear regression in each grid for all the variables. We then derived the ensemble mean anomalies based on the eleven models (Table 1). We further smoothed terrestrial carbon fluxes and climate anomalies using the 3-month running average.

In the spatial correlation coefficient calculation, since the models accounted for varying soil depths, which caused divergence in magnitudes of simulated MRSO, we consistently standardized NEP, surface air

temperature, and soil moisture anomalies in each grid for all models, with the following formula:

$$Z - \text{Score} = \frac{X - \bar{X}}{\sigma} \quad (2)$$

where X and \bar{X} denote the original anomalous variation and time average, respectively. σ represents the standard deviation of the anomalous variation.

2.4. Definitions of climate events

We adopted the Oceanic Niño Index (ONI) (Fig. 1a) to define ENSO events. The ONI is the 3-month running mean SST anomaly for the Niño 3.4 region ($5^\circ\text{N}-5^\circ\text{S}$, $120^\circ\text{E}-170^\circ\text{W}$). Events are defined as five consecutive overlapping 3-month periods at or above the $+0.5$ K anomaly for warm (El Niño) events and at or below the -0.5 K anomaly for cool (La Niña) events. The event severity level can be further categorized into weak (0.50 to 0.99 SST anomaly), moderate (1.00 to 1.49 SST anomaly), strong (1.50 to 1.99 SST anomaly) and very strong (≥ 2.00 SST anomaly). To be classified as a certain level, an event must equal or exceed the threshold for at least three consecutive overlapping 3-month periods.

For IOD events, we used the Indian Ocean Dipole Mode Index (DMI) (Saji et al., 1999), which was calculated from the SST difference between the western equatorial Indian Ocean ($10^\circ\text{S}-10^\circ\text{N}$, $50^\circ\text{E}-70^\circ\text{E}$) and the south-eastern equatorial Indian Ocean ($10^\circ\text{S}-0^\circ\text{N}$, $90^\circ\text{E}-110^\circ\text{E}$) (Fig. 1b).

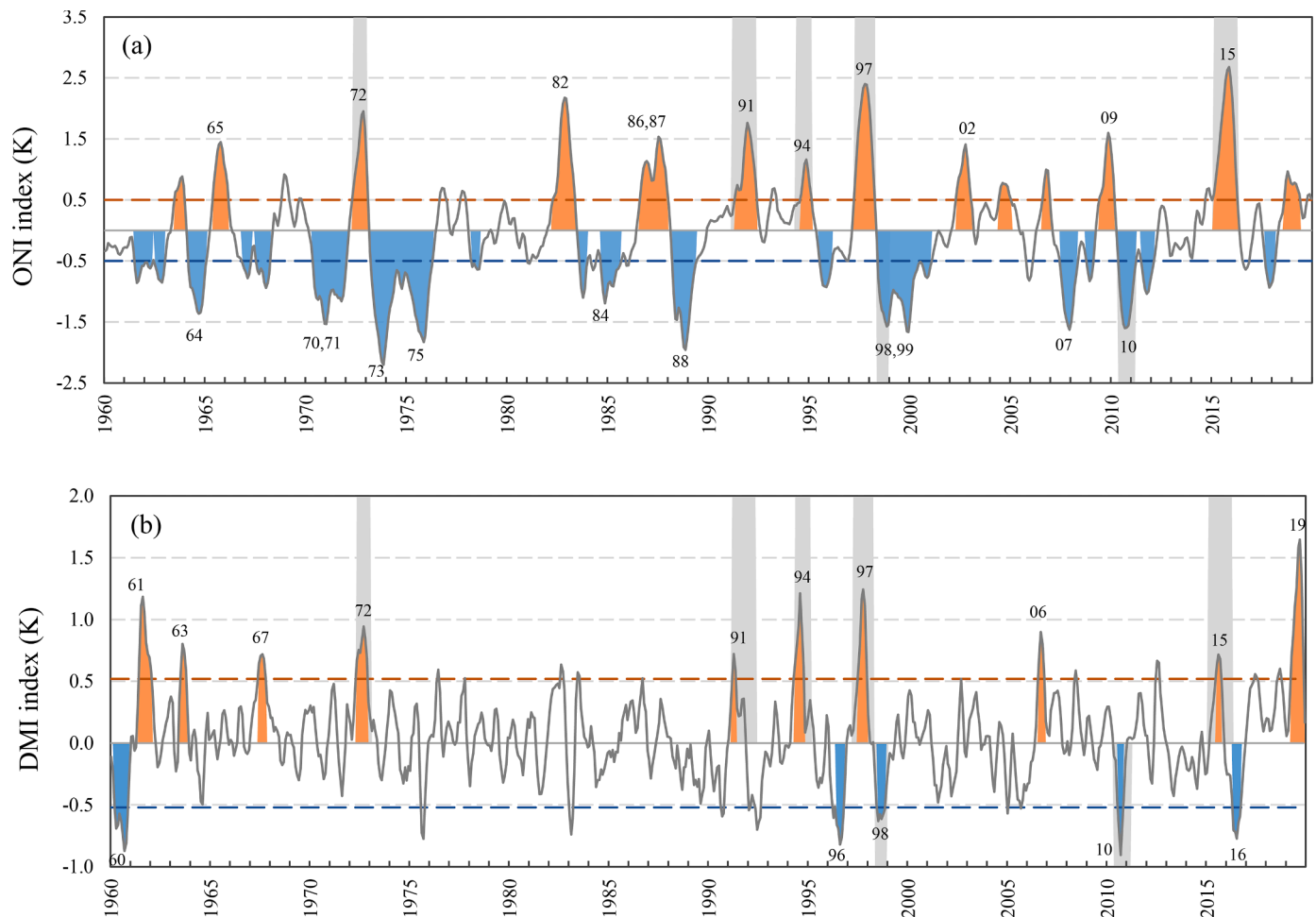


Fig. 1. Time series of Oceanic Niño Index (ONI) (a) and Dipole Mode Index (DMI) (b) from 1960 to 2019. All El Niño events are filled with orange, and La Niña events are filled with blue in (a). Similarly, the positive IOD (pIOD) events are filled with orange and negative IOD (nIOD) events are filled with blue in (b). The moderate, strong, and very strong ENSO events, and all IOD events are denoted by a two-digit year. The red and blue dotted lines in (a) and (b) represent the positive and negative thresholds for ENSO and IOD, respectively. Years with the simultaneous ENSO and IOD activity are marked with the gray background.

The standard deviation of DMI in SON (0.52 K from 1960 to 2019) was used as the criterion for IOD events. A pIOD event occurs when the absolute value of DMI is greater than or equal to 0.52 K for three consecutive 3-month periods. Accordingly, a strong pIOD event in this study is defined if a DMI value is greater than two standard deviations (1.04 K).

2.5. Composite analysis

In counting the years of ENSO events, we retained years of ENSO events of moderate intensity and above due to the high occurrence frequency. On the other hand, we kept all the years of IOD events because of fewer events. We classified individual events and compound events in Table 2. The compound event in this study mainly refers to the El Niño & pIOD and La Niña & negative IOD (nIOD). In addition, we discarded the year of 1991 because of the strong eruption of Mount Pinatubo, which greatly affected the global carbon cycle (Mercado et al., 2009). TRENDY models were also unable to capture this signal well, with most TBMs generally lacking consideration of changing light quality (diffuse radiation fertilization) (Wang et al., 2016).

According to the classifications of climate events (Table 2), we performed the composite analysis using data from all years for an event classification. Since the intensity of the two types of events was relatively low in June-July-August (JJA), we mainly analyzed and discussed seasonally averaged anomalies in September-October-November (SON) (yr0), December(yr0)-January(yr1)-February(yr1) (DJF), and March-April-May (MAM) in the following year (yr1) (Fig. 2), which was in accord with the behaviors that IOD and ENSO events ordinarily peak in SON and DJF, respectively (Saji et al., 1999; Trenberth et al., 2002; Wang et al., 2018). The Student's *t*-test was employed to estimate the significance levels in the composite analysis. However, due to the limited number of pIOD, nIOD, and La Niña & nIOD events (≤ 3 events, Table 2), we only performed the significance test for the El Niño, La Niña, and El Niño & pIOD events.

2.6. Disentangling the individual effects

We constructed a simple linear regression model to understand the individual effects of ENSO and IOD in the specific compound event. In the early stage of an ENSO or IOD event, vegetation may not exhibit abnormalities immediately due to its resistance to environmental changes and self-regulation. Vegetation anomalies tend to occur at a certain time after the event (perhaps a month to a few months, depending on the type of vegetation). With the development of the event, vegetation would be affected by both the previous legacy effects and the concurrent effects. Therefore, concurrent and previous effects of events were both simply included in constructing the linear model. The model can be expressed as

$$NEP_{ij}^c = \alpha_{ij}^c \cdot DMI^c + \alpha_{ij}^l \cdot DMI^l + \beta_{ij}^c \cdot ONI^c + \beta_{ij}^l \cdot ONI^l + e_{ij} \quad (3)$$

where DMI and ONI represent Dipole Mode Index and Oceanic Niño Index, respectively. The superscripts of *c* and *l* denote their values in the concurrent and previous seasons, respectively. The slopes of α and β

Table 2
Occurrence years of individual and compound events from 1960 to 2019.

Events	Years
El Niño	1965, 1982, 1986, 1987, 2002, 2009
La Niña	1964, 1970, 1971, 1973, 1975, 1984, 1988, 1999, 2007
pIOD	2019
nIOD	1960, 1996, 2016
El Niño & pIOD	1972, 1994, 1997, 2015
El Niño & nIOD	–
La Niña & pIOD	–
La Niña & nIOD	1998, 2010

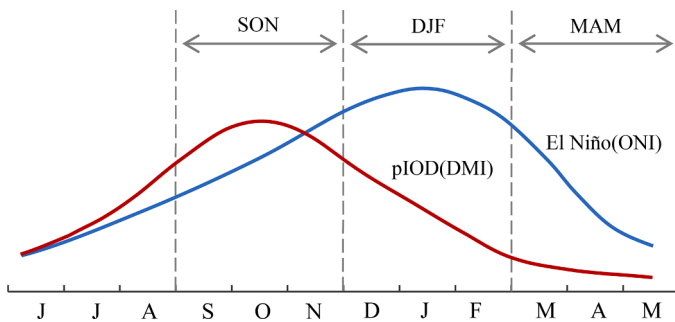


Fig. 2. Schematic diagram for the seasonal composite analysis. The red and blue lines denote the evolving processes of a pIOD event and an El Niño event, respectively.

represent the sensitivities of NEP to these indices. The subscripts of *i* and *j* represent the locations on a grid at $1^\circ \times 1^\circ$ spatial resolution. Therefore, we regarded the terms of $\alpha_{ij}^c \cdot DMI^c$ and $\beta_{ij}^c \cdot ONI^c$ as the concurrent effects of IOD and ENSO, and the terms of $\alpha_{ij}^l \cdot DMI^l$ and $\beta_{ij}^l \cdot ONI^l$ as the legacy effects of IOD and ENSO in the previous season. *e* represents the residual, such as effects of atmospheric circulation other than ENSO and IOD.

3. Results and discussion

3.1. Tropical NEP anomalies and their drivers in compound events

3.1.1. Differences in spatial patterns

We find that IOD events played a more important role in compound events relative to ENSO during SON when IOD peaked (Figs. 3e and n). Specifically, the anomalous carbon absorption occurred in El Niño in the vicinity of $20^\circ S$ in South America, and over southern Africa (Fig. 3a), while the anomalous carbon release occurred there in pIOD (Fig. 3d). However, NEP in the compound events there showed anomalous release, indicating the dominant role of pIOD (Fig. 3e). In contrast, in the equatorial region of South America and India, NEP showed the anomalous carbon release in El Niño and anomalous carbon uptake in pIOD, while anomalous carbon release in the compound events, showing the dominant role of El Niño. Further, El Niño and pIOD did not always cancel out each other in every region. For example, anomalous carbon uptake over eastern Africa and anomalous carbon release over the Indo-China peninsula and most of Australia resulted from the additive effect of pIOD and El Niño in the compound events (Figs. 3a, d, and e). These characteristics were basically reflected of opposite sign in La Niña & nIOD compound events, with some small differences in certain places like southern Africa (Fig. 3n).

In DJF, ENSO got mature (Fig. 2). Here, we analyzed La Niña, nIOD, and their compound events (Figs. 3i, l, and o) considering the availability of their positive counterparts. In this period, the magnitude of NEP anomalies increased from their amplifying effects, notably over most of South America, eastern and southern Africa, Indonesia, and Australia. However, the slightly negative NEP anomalies over western Africa were dominated by the nIOD. In addition, the positive NEP anomalies over India and negative anomalies over the Indo-China peninsula in the compound events were different from those in individual events (La Niña and nIOD, Figs. 3i and l), perhaps because the cases of La Niña & nIOD events were too few (only two years) to be fully representative.

In MAM, the impact of La Niña slightly weakened (Fig. 3j). NEP anomalies were influenced by the amplifying effects of La Niña and nIOD mainly over eastern and southern Africa, and the Indo-China peninsula (Figs. 3j, m, and p). In contrast, positive NEP anomalies were predominantly controlled by La Niña over South America and northeastern Australia, whereas negative NEP anomalies over western Africa were controlled by nIOD.

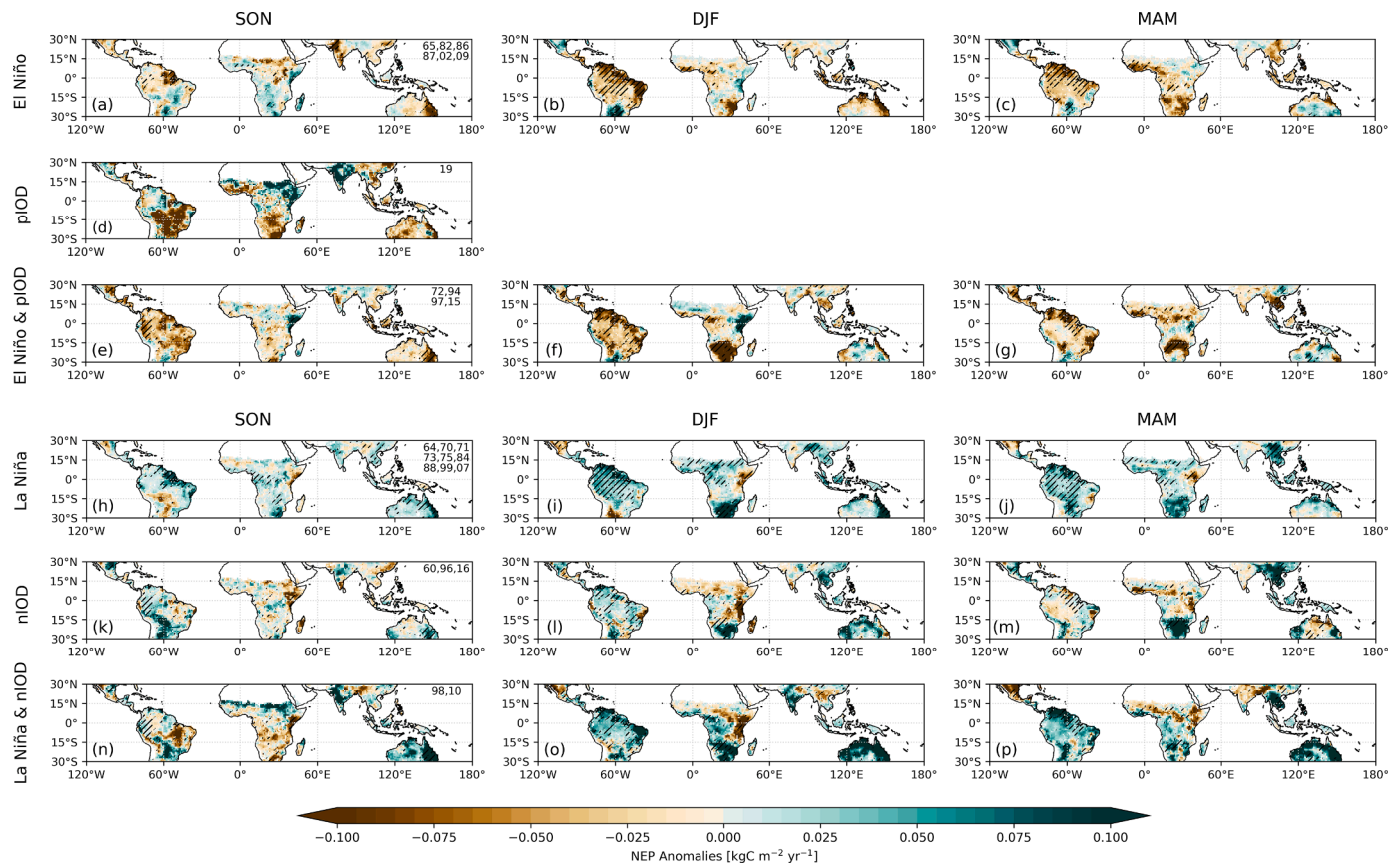


Fig. 3. Spatial distributions of seasonal composite tropical net ecosystem productivity (NEP) anomalies for different event classes. The black slashes indicate areas with significance at $p \leq 0.1$ relative to non-event years from 1960 to 2019 based on the Student's two-sample t -test. Numbers in subplots (first column) denote the years for composite analysis. The spatial patterns of compound events (El Niño & pIOD and La Niña & nIOD) in different seasons can be different from those of single events. Compared with single events, the amplifying effects in some regions between IOD and ENSO could show stronger impacts, while their counterbalancing could make the NEP anomalies close to neutral or dominated by the stronger event. Here we only compared the spatial differences qualitatively among different classifications because of different years used in composite analysis.

We calculated the total NEP anomalies for the pan-tropics (Trop, 30°S - 30°N) and three sub-continents including tropical South America (TSA, 120°W - 25°W), tropical Africa (TAF, 25°W - 60°E), and tropical Asia-Pacific (TAP, 60°E - 180°E). NEP anomalies over the pan-tropics and these three sub-continents induced by El Niño, pIOD, and El Niño & pIOD were always negative, whereas the anomalies induced by La Niña, nIOD, and La Niña & nIOD were always positive (Fig. 4). Owing to the different years of cases (Table 2), we focus on their phases (the seasons

with the maximum/minimum NEP anomaly) in different classifications.

We found that the minimum NEP anomalies in El Niño (the maximum NEP anomalies in La Niña) over the tropics generally occurred in DJF. But there were some exceptions. The minimum NEP over TAF in El Niño occurred in MAM (Fig. 4a) which was consistent with the vast areas of negative NEP anomalies (Fig. 3c). And the NEP anomaly of TSA in La Niña was slightly higher (by approximately 0.01 PgC yr^{-1}) in MAM than in DJF (Fig. 4d), possibly because of the smaller negative

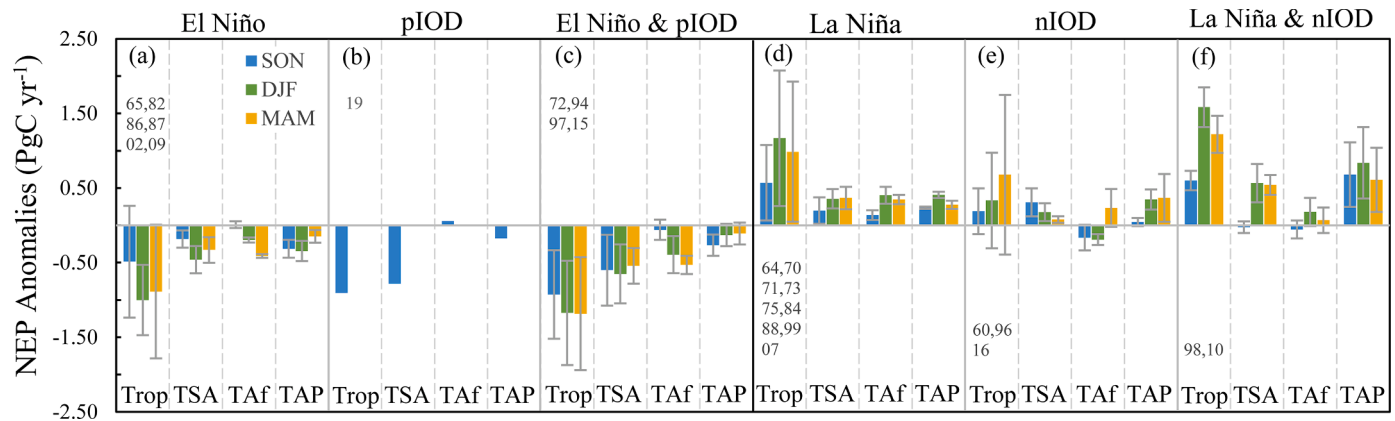


Fig. 4. The total seasonal anomalies of NEP in different classified events for tropics (abbreviated as "Trop"), tropical South America ("TSA"), tropical Africa ("TAF"), tropical Asia and Pacific ("TAP"), respectively. The error bars represent the standard deviation of different events in the composite analysis. Numbers in each subplot denote the selected years.

anomaly in the vicinity of 20°S during MAM (Fig. 3g). In IOD (mainly nIOD here) events, the maximum NEP anomalies mainly occurred in MAM except TSA in SON (Fig. 4e). Additionally, it is worth noting that anomalous carbon release occurred in SON and DJF in nIOD events while anomalous carbon uptake occurred in MAM over TAF.

During El Niño & pIOD events, the tropical negative NEP anomaly in MAM was slightly lower (by approximately 0.01 PgC yr⁻¹) than that in DJF. Interestingly, seasons with minimum negative NEP anomalies were distinct in the three sub-regions, showing the minimum values in DJF over TSA, MAM over TAF, and SON over TAP, respectively (Fig. 4c), which can be seen in their spatial patterns (Figs. 3e–g). However, in La Niña & nIOD events, the maximum NEP anomalies were all positive and occurred in DJF (Fig. 4f).

These quantitative results showed that the phases of NEP anomalies in compound events were different from those in single ENSO and IOD events. It potentially indicated that changes of NEP anomalies in compound events were influenced by the interaction of ENSO and IOD.

3.1.2. Biological processes and climate drivers

In general, GPP dominated NEP anomalies rather than TER over the pan-tropics and sub-continents in individual and compound events (Figs. 5 and S1). Specific characteristics during El Niño & pIOD and La Niña & nIOD are discussed below.

During the composite El Niño & pIOD event, the minimum pan-tropical NEP anomaly occurred in MAM with the magnitude of -1.18 ± 0.76 PgC yr⁻¹, caused by a greater reduction of GPP (-1.70 ± 0.53 PgC yr⁻¹) than that of TER (-0.66 ± 0.15 PgC yr⁻¹) (Fig. 5a). Significant regional differences existed, as mentioned above. In TSA, seasonal differences among NEP, GPP, and TER anomalies were small owing to insignificant changes in temperature and soil moisture anomalies (Fig. 6). The minimum NEP anomaly occurred in DJF with the magnitude of -0.65 ± 0.30 PgC yr⁻¹, while the minimum GPP (-0.79 ± 0.42 PgC yr⁻¹) and TER (-0.31 ± 0.14 PgC yr⁻¹) anomalies happened in MAM (Fig. 5b). In TAF, warmest temperature and driest soil moisture occurred over southern Africa in DJF (Figs. 6b and h), which could inhibit photosynthesis and enhance respiration (Figs. S2f and S3f), as also suggested by previous studies (Wang et al., 2016; Zeng et al., 2005), causing strong anomalous carbon release in the area (Fig. 3f). Simultaneously, wettest anomalous conditions occurred over eastern Africa (Fig. 6h), which could strongly enhance GPP (Fig. S2f), causing significant anomalous carbon uptake (Fig. 3f). The strong spatial compensation of TAF in DJF caused the occurrence of minimum values of NEP, GPP, and TER in MAM, with anomalies of -0.53 ± 0.27 , -0.81 ± 0.53 , and -0.34 ± 0.35 PgC yr⁻¹, respectively (Fig. 5c). There were more

positive and negative cancellations of NEP anomalies within Africa. Perhaps because Africa is distributed symmetrically around the equator, the climate is different between the north and south of the equator in the same season, and the vegetation is affected differently. In TAP, the minimum NEP, GPP, and TER anomalies all occurred in SON with their magnitudes of -0.27 ± 0.17 , -0.59 ± 0.42 , and -0.34 ± 0.27 PgC yr⁻¹, respectively (Fig. 5d). Spatially, the widespread drought over Indonesia and Australia mainly contributed to these anomalies (Figs. 3e, S2e, S3e, and 6g).

During its counterpart, La Niña & nIOD, the maximum composite pan-tropical NEP anomaly occurred in DJF which was caused by more enhancement of GPP (2.28 ± 0.35 PgC yr⁻¹) than that of TER (0.97 ± 0.16 PgC yr⁻¹) (Fig. 5e). For the three sub-continents, although the maximum NEP anomalies consistently occurred in DJF, with composite total anomalies of 0.57 ± 0.05 , 0.18 ± 0.20 , and 0.84 ± 0.12 PgC yr⁻¹ over TSA, TAF, and TAP, respectively (Figs. 4f and 5f–h), the maximum anomalies of GPP and TER appeared in different seasons. Specifically, in TSA, GPP and TER were both inhibited in SON (Figs. 5f, S2n, and S3n) owing to drier and warmer conditions (Figs. 6d and j). However, they were enhanced in the following seasons associated with lower temperature and wetter soil moisture (Figs. 6e, f, k, and l), causing relatively stronger positive anomalies in GPP and TER in DJF than in MAM (Fig. 5f). In TAF, although GPP and TER anomalies had strongest positive or negative values in specific regions in DJF (such as eastern and southern Africa) among these three seasons (Figs. S2o and S3o), the strong spatial compensation resulted in minimum negative total anomalies in GPP (-0.29 ± 0.72 PgC yr⁻¹) and TER (-0.31 ± 0.43 PgC yr⁻¹) in MAM (Fig. 5g). In TAP, the maximum total GPP (1.63 ± 0.07 PgC yr⁻¹) and TER (0.95 ± 0.10 PgC yr⁻¹) anomalies happened in SON (Fig. 5h), mainly located over India and Australia (Figs. S2n and S3). They were largely caused by wetter soil moisture (Fig. 6j).

We further calculated spatial correlation coefficients between NEP and temperature/soil moisture to explore which climate factor played the most important role in shaping the NEP anomalous patterns in different classifications and seasons (Table 3 and S1). Due to the strong spatial autocorrelation, it was difficult for us to calculate the degree of freedom and give out the reasonable significance. We considered that the spatial correlation coefficient calculated from the composite was significant when the signs of correlation coefficients calculated from all the single cases were consistent with that from the composite.

In El Niño & pIOD, the NEP anomalous patterns consistently had higher spatial correlation coefficients with soil moisture in different seasons over the entire tropics and three sub-continents, indicating the greater importance of soil moisture (Table 3). This was somewhat

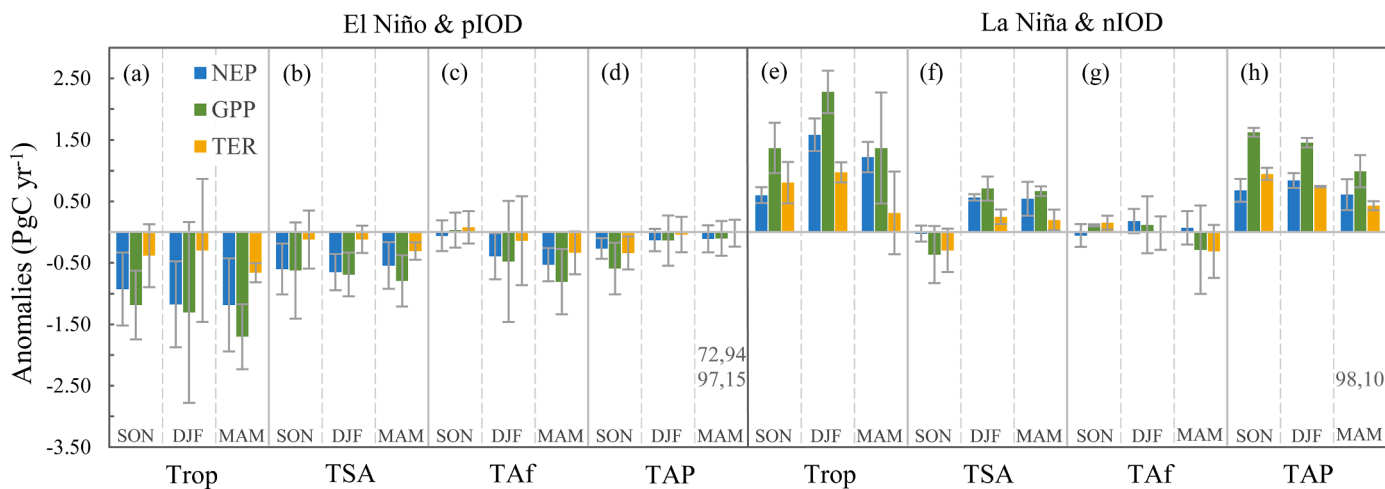


Fig. 5. Total seasonal anomalies of NEP, gross primary productivity (GPP), and total ecosystem respiration (TER) in El Niño & pIOD and La Niña & nIOD events. The error bars represent the standard deviation of different variables in different events in each classification for the composite analysis. Numbers in (d) and (h) denote the selected years.

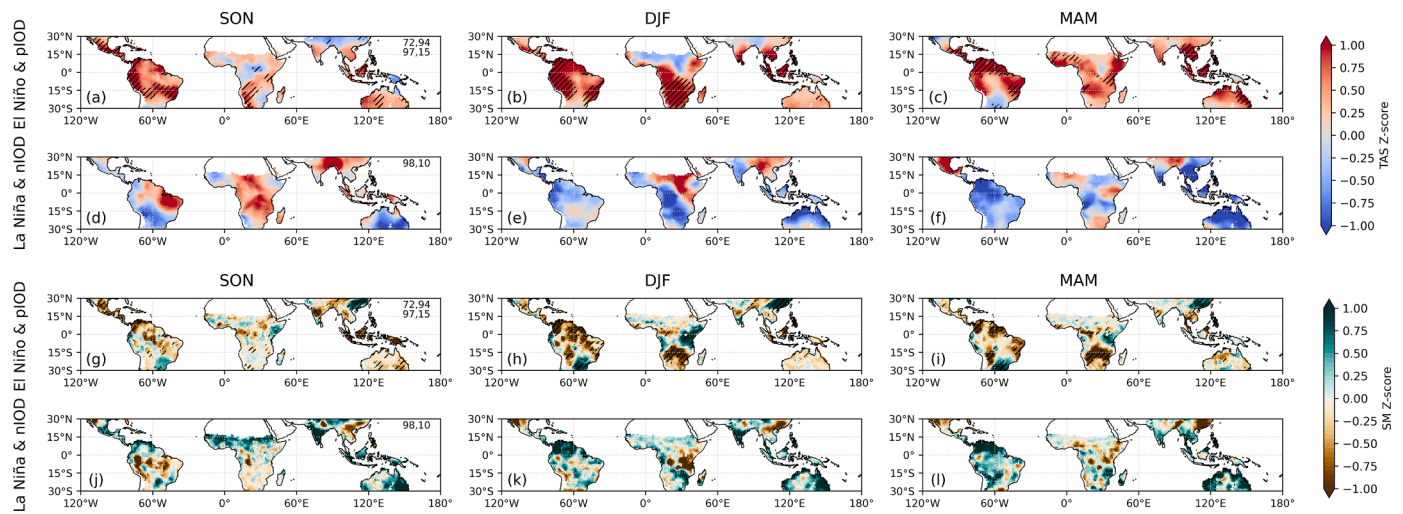


Fig. 6. Spatial distributions of seasonal composite tropical normalized climate anomalies. (a-c) Normalized temperature in El Niño & pIOD. (d-f) Normalized temperature in La Niña & nIOD. (g-i) Normalized soil moisture in El Niño & pIOD. (j-l) Normalized soil moisture in La Niña & nIOD. The black slashes indicate areas with significance at $p \leq 0.1$ relative to non-event years from 1960 to 2019 based on the Student's two-sample t -test. Numbers in subplots (first column) denote the years for composite analysis.

different from the mechanisms in El Niño which showed a higher correlation coefficient between NEP and temperature in MAM over the entire tropics (Table S1). For La Niña & nIOD over the pan-tropics, soil moisture played a more important role in SON, while temperature and soil moisture had comparable effects in DJF and MAM (Table 3). It was also different from the individual events (La Niña or nIOD), especially in DJF (Table S1). For the sub-continents, except TSA in DJF and TAF in SON and MAM, other regions were more controlled by temperature. These correlation coefficients suggested asymmetric effects of soil moisture and temperature on NEP anomalies during El Niño & pIOD and La Niña & nIOD, as suggested by a previous study for El Niño and La Niña (Fang et al., 2017).

3.2. Revisiting the tropical carbon flux anomalies during 1997/98

In the above content, we mainly qualitatively discussed ENSO and IOD effects in compound events. However, since the events occurred in different years, we cannot directly determine individual contributions from ENSO and IOD. Here, we adopt the multi-variate linear regression model (Eq. (3)) to estimate individual contributions for specific cases. The *F*-test indicates that this simple linear model has good performance over most tropical vegetated areas (Fig. S4). Further, total NEP anomalies for all the six compound events (Table 2) were calculated by this linear model over the entire tropics and three sub-continents, and the results generally matched well with the multi-model simulated ensemble NEP anomalies (Fig. S5). Among these six compound events, the extreme El Niño and pIOD events simultaneously occurred in 1997/98 (Fig. 1 and Table 2), with the maximum magnitude of NEP anomalies (Fig. S6), which had significant impacts on the carbon cycle in the tropics. Hence, we focus on their individual effects for the 1997/98 compound event.

3.2.1. NEP anomalies during SON in 1997

Compared with the raw TBM NEP anomalies (Fig. 7a), the calculated NEP anomalies can capture most of the characteristics, except some deviations over southern Africa, India, and western Australia (Fig. 7b),

with their root mean square errors (RMSE) of $0.05 \text{ kgC m}^{-2} \text{ yr}^{-1}$ and spatial correlation coefficient of 0.46. The decomposed spatial patterns of contributions from the pIOD and El Niño showed obvious different patterns, to a large extent consistent with patterns in the composite El Niño and pIOD (Figs. 3a and d). In SON, contributions from the pIOD in 1997 was dominated by the concurrent pIOD effect (Fig. 7e), whereas the legacy effect of the pIOD in the preceding season was nearly neutral because pIOD developed in July and peaked in October (Fig. 7g). In contrast, both concurrent and legacy effects of the El Niño (developed in May 1997) were strong (Figs. 7f and h).

In detail, over TSA, the calculated total NEP anomaly by the simple regression model was $-0.68 \pm 0.41 \text{ PgC yr}^{-1}$, somewhat smaller than the raw NEP anomaly of $-0.92 \pm 0.00 \text{ PgC yr}^{-1}$ (Fig. 7i). It was composed of -0.34 ± 0.15 and $-0.35 \pm 0.32 \text{ PgC yr}^{-1}$ contributed by the pIOD and El Niño, respectively. Spatially, negative NEP anomalies dominated by pIOD were located in the south and by El Niño in the north (Fig. 7c), as revealed in Fig. 3. The decomposed pIOD-induced NEP anomalies mainly originated from its concurrent impact ($-0.30 \pm 0.14 \text{ PgC yr}^{-1}$). However, the decomposed El Niño-induced NEP anomalies were significantly influenced by concurrent ($0.67 \pm 0.45 \text{ PgC yr}^{-1}$) and legacy effects ($-1.02 \pm 0.59 \text{ PgC yr}^{-1}$), showing that the concurrent effect partially cancelled out the legacy effects.

The total NEP anomalies over TAF were small, with comparable magnitudes of $-0.02 \pm 0.00 \text{ PgC yr}^{-1}$ in raw and $-0.05 \pm 0.15 \text{ PgC yr}^{-1}$ in calculated NEP anomalies, largely owing to the compensation of the pIOD and El Niño effects. The total NEP anomaly caused by the pIOD was positive with its magnitude of $0.5 \pm 0.19 \text{ PgC yr}^{-1}$, while that caused by El Niño was negative with a magnitude of $-0.54 \pm 0.14 \text{ PgC yr}^{-1}$, composing of 0.35 ± 0.34 and $-0.89 \pm 0.41 \text{ PgC yr}^{-1}$ estimated by the concurrent and legacy effects, respectively.

Over TAP, the estimated total NEP was $-0.50 \pm 0.46 \text{ PgC yr}^{-1}$, caused by the pIOD-induced $-0.08 \pm 0.00 \text{ PgC yr}^{-1}$ and El Niño-induced $-0.42 \pm 0.37 \text{ PgC yr}^{-1}$. This estimation was stronger than the raw NEP anomaly of $-0.08 \pm 0.25 \text{ PgC yr}^{-1}$, and probably resulted from an overestimation of the role of El Niño in our linear regression model.

Table 3

Spatial correlation coefficients of NEP anomalies with surface air temperature (Tas) and soil moisture (SM) anomalies in different events and seasons. All the data used for calculation were standardized. The values in brackets show the minimum and maximum spatial correlation coefficients for the selected cases listed in Table 1. The spatial correlation coefficient calculated from the composite was significant when the signs of correlation coefficients calculated from all the single cases were consistent with that from the composite, and these significant spatial correlation coefficients were shown in bold.

El Niño & pIOD		TSA		TAF		TAP		
Trop	SM	Tas	SM	Tas	SM	Tas	SM	Tas
SON	0.46 (0.48~0.61)	-0.42 (-0.47~-0.15)	0.34 (0.31~0.57)	-0.26 (-0.55~-0.21)	0.52 (0.48~0.69)	-0.11 (-0.48~-0.02)	0.53 (0.22~0.49)	-0.42 (-0.38~-0.17)
DJF	0.57 (0.43~0.53)	-0.46 (-0.44~-0.20)	0.58 (0.36~0.56)	-0.41 (-0.45~-0.24)	0.67 (0.45~0.66)	-0.47 (-0.60~-0.18)	0.22 (0.25~0.48)	-0.21 (-0.47~-0.12)
MAM	0.66 (0.48~0.62)	-0.38 (-0.55~-0.26)	0.64 (0.34~0.62)	-0.51 (-0.51~-0.28)	0.69 (0.46~0.67)	-0.19 (-0.62~-0.09)	0.59 (0.50~0.70)	-0.42 (-0.56~-0.12)

3.2.2. NEP anomalies during DJF in 1997/98

In DJF, except for some deviations over India and northeastern Australia, the spatial pattern of the calculated NEP well matched the spatial pattern of the raw NEP anomalies, with an RMSE of $0.05 \text{ kgC m}^{-2} \text{ yr}^{-1}$ and spatial correlation coefficient of 0.70 (Figs. 8a and b). We can find that both the concurrent and legacy impacts of the pIOD and El Niño played significant roles. In TSA, the linear model captured well the spatial features, showing a comparable total in negative NEP anomalies ($-0.76 \pm 0.43 \text{ PgC yr}^{-1}$) with the raw value ($-0.75 \pm 0.00 \text{ PgC yr}^{-1}$). This negative NEP anomaly was dominated by El Niño with an impact of $-0.58 \pm 0.38 \text{ PgC yr}^{-1}$. Specifically, the concurrent and legacy contributions of El Niño had comparable magnitudes of impacts of -0.30 ± 0.43 and $-0.28 \pm 0.55 \text{ PgC yr}^{-1}$, respectively. Even so, their contributions in spatial distributions had different characteristics (Figs. 8f and h). In addition, the negative NEP anomalies mainly caused by the pIOD legacy (pIOD disappeared in January) partially offset the effect of the El Niño in the south (Figs. 8c and g).

In TAF, although the spatial patterns were similar, showing the strong anomalous carbon uptake over the eastern Africa and anomalous carbon release over the central and southern Africa (Figs. 8a and b), the calculated total NEP anomaly was $-0.25 \pm 0.26 \text{ PgC yr}^{-1}$, in contrast with $0.17 \pm 0.00 \text{ PgC yr}^{-1}$ in the raw NEP anomaly. The pIOD, mainly from the legacy effects, resulted in total positive NEP anomaly of $0.35 \pm 0.47 \text{ PgC yr}^{-1}$, while El Niño resulted in total negative NEP anomaly ($-0.60 \pm 0.35 \text{ PgC yr}^{-1}$), mainly due to legacy effects in the north and concurrent effects in the south (Figs. 8f and h).

In TAP, the estimated NEP anomaly was $-0.54 \pm 0.40 \text{ PgC yr}^{-1}$, stronger than $-0.02 \pm 0.00 \text{ PgC yr}^{-1}$ in raw data. This departure was probably due to the overestimation of anomalous carbon release over India and northeastern Australia (Figs. 8a and b), mainly caused by the impacts of El Niño (Fig. 8d). In general, the pIOD, mainly from the concurrent impacts, caused anomalous carbon uptake north of 20°N and eastern Australia (Fig. 8c), making the total positive NEP of $0.07 \pm 0.14 \text{ PgC yr}^{-1}$. The concurrent effects of El Niño were superimposed on its legacy effects, resulting in a total negative NEP anomaly of $-0.61 \pm 0.32 \text{ PgC yr}^{-1}$ (-0.14 ± 0.45 and $-0.47 \pm 0.51 \text{ PgC yr}^{-1}$ by concurrent and legacy effects, respectively).

3.2.3. NEP anomalies during MAM in 1998

During MAM, the spatial pattern of the estimated NEP anomalies based on the linear model also matched well with the raw data, with the

RMSE of $0.06 \text{ kgC m}^{-2} \text{ yr}^{-1}$ and spatial correlation coefficient of 0.68 (Figs. 9a and b). Changes in NEP anomalies were predominantly controlled by El Niño throughout the tropics, except that pIOD dominated over eastern parts of South America, eastern Africa, and north-eastern Australia (Figs. 9c and d). The concurrent effects of the pIOD and El Niño were close to zero (Figs. 9e and f). Hence, NEP anomalies were mainly influenced by their legacy effects, in which El Niño played a greater role (Figs. 9h and i). In TSA, a negative NEP anomaly was mainly caused by El Niño legacy with the value of $-0.56 \pm 0.28 \text{ PgC yr}^{-1}$. In TAF, pIOD had a stronger effect over the eastern Africa, causing total positive NEP anomaly of $0.22 \pm 0.22 \text{ PgC yr}^{-1}$, partially offsetting the negative effect of El Niño ($-0.65 \pm 0.20 \text{ PgC yr}^{-1}$). In TAP, although the total contribution of pIOD was close to zero ($0.02 \pm 0.29 \text{ PgC yr}^{-1}$), it can be seen that pIOD caused the obvious positive NEP anomalies in eastern Australia. And El Niño caused $-0.40 \pm 0.35 \text{ PgC yr}^{-1}$ NEP anomaly, composing of -0.06 ± 0.21 and $-0.34 \pm 0.32 \text{ PgC yr}^{-1}$ induced by the concurrent and legacy, respectively.

3.3. Implications and limitation

It is well known that large-scale atmospheric circulation oscillations can exert abiotic stresses on biota affecting the terrestrial carbon cycle. Many previous literatures have extensively studied the impacts of ENSO (especially El Niño) events on tropical terrestrial carbon flux variations (Bowman et al., 2017; Liu et al., 2017; Piao et al., 2019; Wang et al., 2016, 2018a, b). In contrast, less attention has been paid to IOD, another mode of air-sea coupling, and its role in regulating terrestrial carbon fluxes, with only a limited number of studies focusing on IOD-affected GPP over IO rim countries (Wang et al., 2021; Williams and Hanan, 2011). In the past six decades, there was a high probability for simultaneous IOD and ENSO activity, especially El Niño & pIOD and La Niña & nIOD (Table 2). The spatial patterns of NEP anomalies influenced by the strong interference of simultaneous IOD and ENSO activity had its own characteristics. For example, IOD dominated NEP anomalies over eastern and southern Africa, and the vicinity of 20°S in South America, and enhanced the impacts of ENSO in Australia and Indonesia during SON. The interferences between IOD legacy and ENSO also existed during DJF and MAM (Fig. 3). Therefore, when simultaneous ENSO and IOD activity occurred, we cannot fully understand the changes in tropical terrestrial carbon fluxes if we only consider ENSO events as was conventionally done. Moreover, previous studies have suggested that

La Niña & nIOD		TSA		TAf		TAP	
Trop SM	Tas	SM	Tas	SM	Tas	SM	Tas
0.54 (0.43~0.49)	-0.40 (-0.36~-0.33)	0.40 (0.26~0.38)	-0.46 (-0.43~-0.29)	0.62 (0.48~0.50)	-0.22 (-0.32~-0.05)	0.52 (0.40~0.56)	-0.53 (-0.52~-0.41)
0.58 (0.46~0.52)	-0.58 (-0.45~-0.41)	0.56 (0.44~0.47)	-0.39 (-0.39~-0.14)	0.46 (0.31~0.48)	-0.56 (-0.53~-0.46)	0.63 (0.42~0.65)	-0.75 (-0.61~-0.40)
0.62 (0.49~0.60)	-0.63 (-0.58~-0.52)	0.69 (0.52~0.57)	-0.74 (-0.61~-0.61)	0.39 (0.43~0.48)	-0.24 (-0.44~-0.22)	0.59 (0.48~0.70)	-0.65 (-0.58~-0.56)

the frequency of extreme pIOD and El Niño events may increase under future greenhouse warming based on the Coupled Model Intercomparison Project phase 5 (CMIP5) multi-model simulations (Cai et al., 2014a, b). Additionally, Kim et al. (2017) pointed out that the sensitivity of interannual variation of tropical terrestrial carbon flux to ENSO will be enhanced under greenhouse warming. Wang et al. (2021) also suggested the larger impacts of IOD on terrestrial GPP in CMIP6 multi-model future projections over certain regions, such as central and eastern Africa, Sumatra, and western and southeastern Australia with enhanced explained variances. Hence, we believe that a comprehensive understanding of the interactive effects of IOD and ENSO events on tropical terrestrial carbon flux variations is fundamental to understanding these future changes in sensitivity and impacts.

There is a large inter-model spread in NEP anomalies in TRENDYv9 TBMs, as mentioned by previous studies (Bastos et al., 2018; Friedlingstein et al., 2020; Wang et al., 2018a), originating from their different parameterizations and processes considered, resulting in large differences in simulated responses of photosynthesis and respiration to CO₂ concentration and climate (Rogers, 2014; Rogers et al., 2017). While we selected some models to partially reduce the uncertainty, we mainly focused on the ensemble result without enough consideration of the individual model performance. Furthermore, although results of the composite analysis based on the ensemble result can explain most of the interactive effects between IOD and ENSO in compound events, uncertainties remained over some regions (e.g. India and the Indo-China peninsula in DJF during La Niña & nIOD; Fig. 3o) because of the limited number of events (only one pIOD event, two La Niña & nIOD events, and three nIOD events). Additionally, a simple linear model was used to calculate the individual contributions of ENSO and IOD in 1997/98 compounds events. The *F*-test demonstrated the model performed well and the calculated results showed a high spatial correlation coefficient with the original data. However, we admitted that there may be some underestimation or overestimation in total carbon fluxes over the sub-continents.

In addition, ENSO can also be divided into eastern Pacific (EP) and Central Pacific (CP) El Niño, with different global teleconnections and different impacts on the terrestrial carbon cycle (Kao and Yu, 2009; Wang et al., 2018a). Therefore, more detailed classification of ENSO types may be suggested for future studies.

4. Conclusion

In this study we comprehensively investigated the interactive effects of ENSO and IOD on the tropical NEP interannual variations both qualitatively and quantitatively by the composite analysis and a multivariate linear regression model from 1960 to 2019. The main conclusions are summarized as follows:

- 1) In compound events, NEP anomalies were affected by the amplifying effects or counterbalancing between ENSO and IOD. In particular, NEP anomalies were dominated by IOD over South America near 20°S and Africa south of the Equator, dominated by ENSO over India and northern South America, and influenced by their amplifying effects over eastern Africa, Indo-China and most of Australia during SON. In DJF, their amplifying effects played the dominant roles, notably over most of South America, eastern and southern Africa, Indonesia, and Australia. In MAM, the influence of IOD legacy effects gradually disappeared, and tropical NEP anomalies were predominantly controlled by ENSO events. These characteristics make the phases of NEP anomalies in compound events different from those in individual ENSO and IOD events.
- 2) Attribution analysis suggested the dominant role of GPP in these NEP anomalies in different seasons rather than TER. However, the effects of temperature and soil moisture played different roles in different events. Specifically, spatial correlation coefficients suggested that NEP anomalies had higher correlation coefficients with soil moisture in El Niño & pIOD, but generally higher correlation coefficients with temperature in La Niña & nIOD.
- 3) For the simultaneous extreme pIOD and El Niño activity in 1997/98, we estimated their individual contributions and found that the pIOD event had the greatest influence during SON, followed by DJF. This is consistent with the results of composite analysis. During the SON in 1997, the individual contributions of pIOD and El Niño were -0.34 ± 0.15 and $-0.35 \pm 0.32 \text{ PgC yr}^{-1}$ in the tropical South America, 0.5 ± 0.19 and $-0.54 \pm 0.14 \text{ PgC yr}^{-1}$ in the tropical Africa, -0.08 ± 0.25 and $-0.42 \pm 0.37 \text{ PgC yr}^{-1}$ in the tropical Asia-Pacific, respectively. Furthermore, during the DJF in 1997/98, the individual contributions of pIOD and El Niño were -0.18 ± 0.15 and $-0.58 \pm 0.38 \text{ PgC yr}^{-1}$ in tropical South America, $0.35 \pm 0.37 \text{ PgC yr}^{-1}$ and $-0.60 \pm 0.35 \text{ PgC yr}^{-1}$ in tropical Africa, $0.07 \pm 0.14 \text{ PgC yr}^{-1}$ and $-0.61 \pm 0.32 \text{ PgC yr}^{-1}$ in tropical Asia-Pacific, respectively.

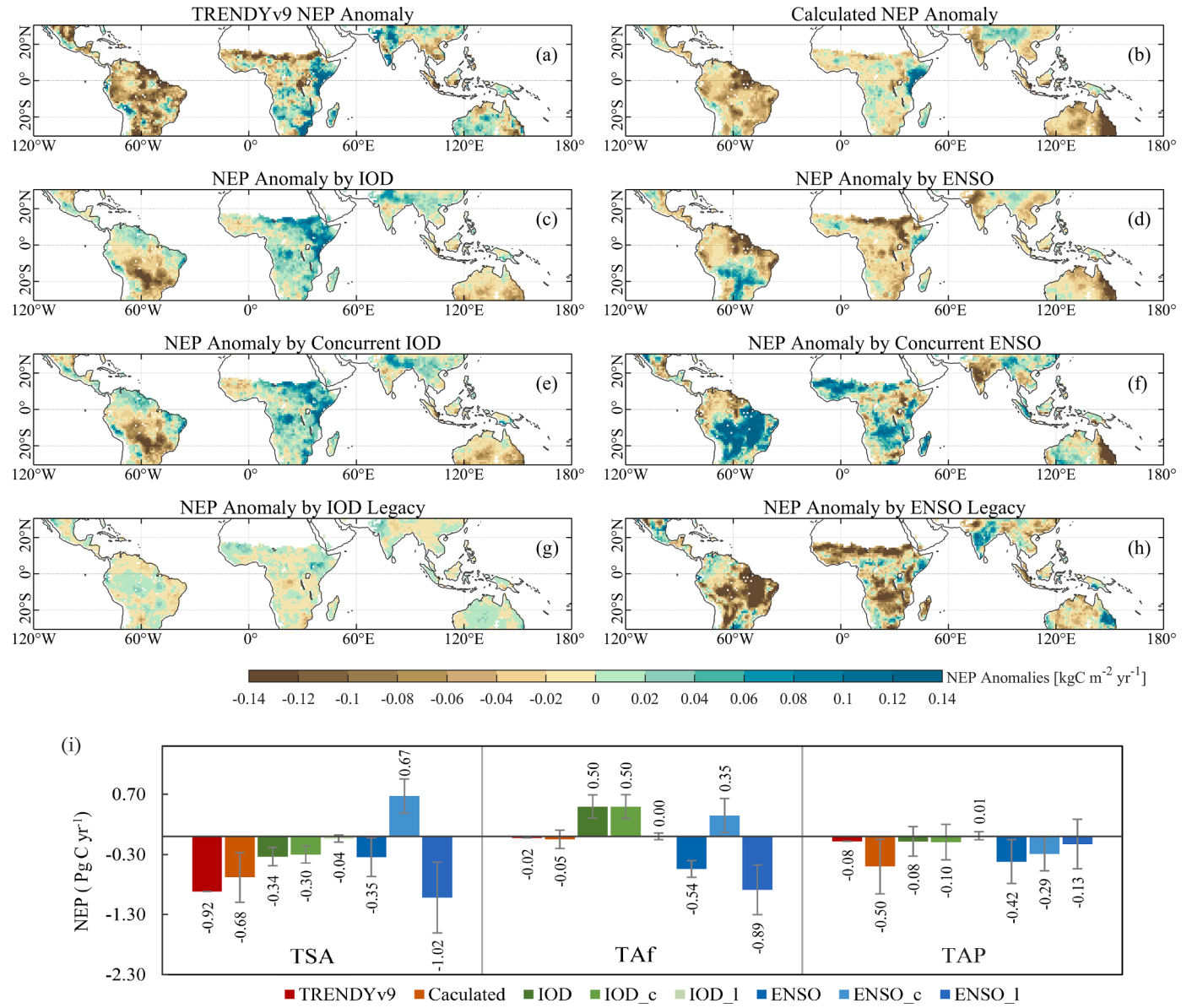


Fig. 7. NEP anomalies during SON in 1997. (a) NEP anomalies originally derived from TRENDYv9 ensemble result. (b) Calculated NEP anomaly derived from the linear regression model. (c) Calculated NEP anomaly affected by the pIOD. (d) Calculated NEP anomaly affected by the El Niño. (e and g) Calculated NEP anomalies influenced by the concurrent and preceding pIOD, respectively. (f and h) Calculated NEP anomalies influenced by the concurrent and preceding El Niño, respectively. (i) Total NEP anomalies caused by the pIOD and El Niño over the three sub-continents: TAS, TAf and TAP. The values in (c) were the sum of values in (e) and (g), and the values in (d) were the sum of values in (f) and (h). The error bars in (i) represent the standard deviation of the results calculated from each TBM.

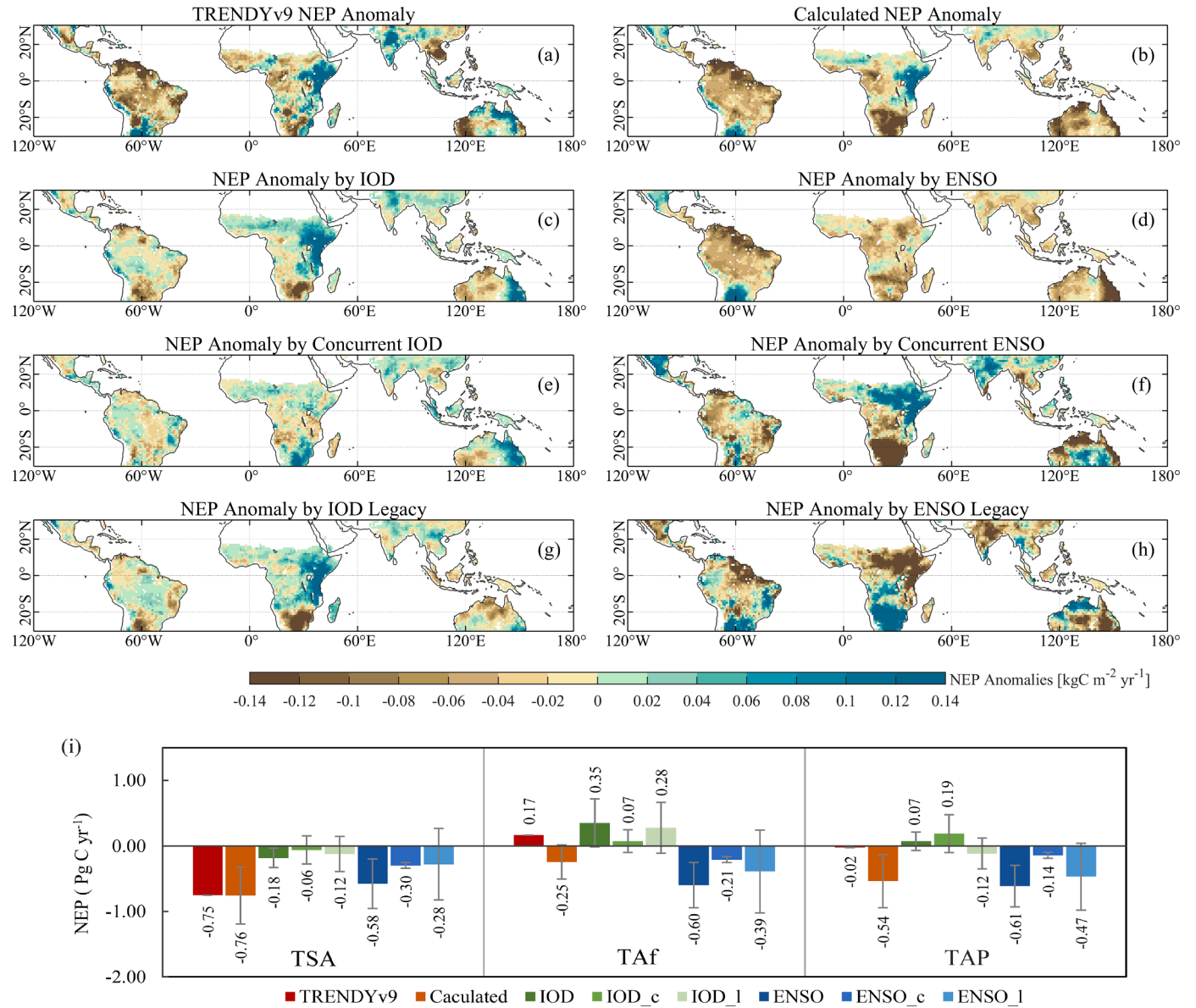


Fig. 8. Same as Fig. 7, but for DJF in 1997/98.

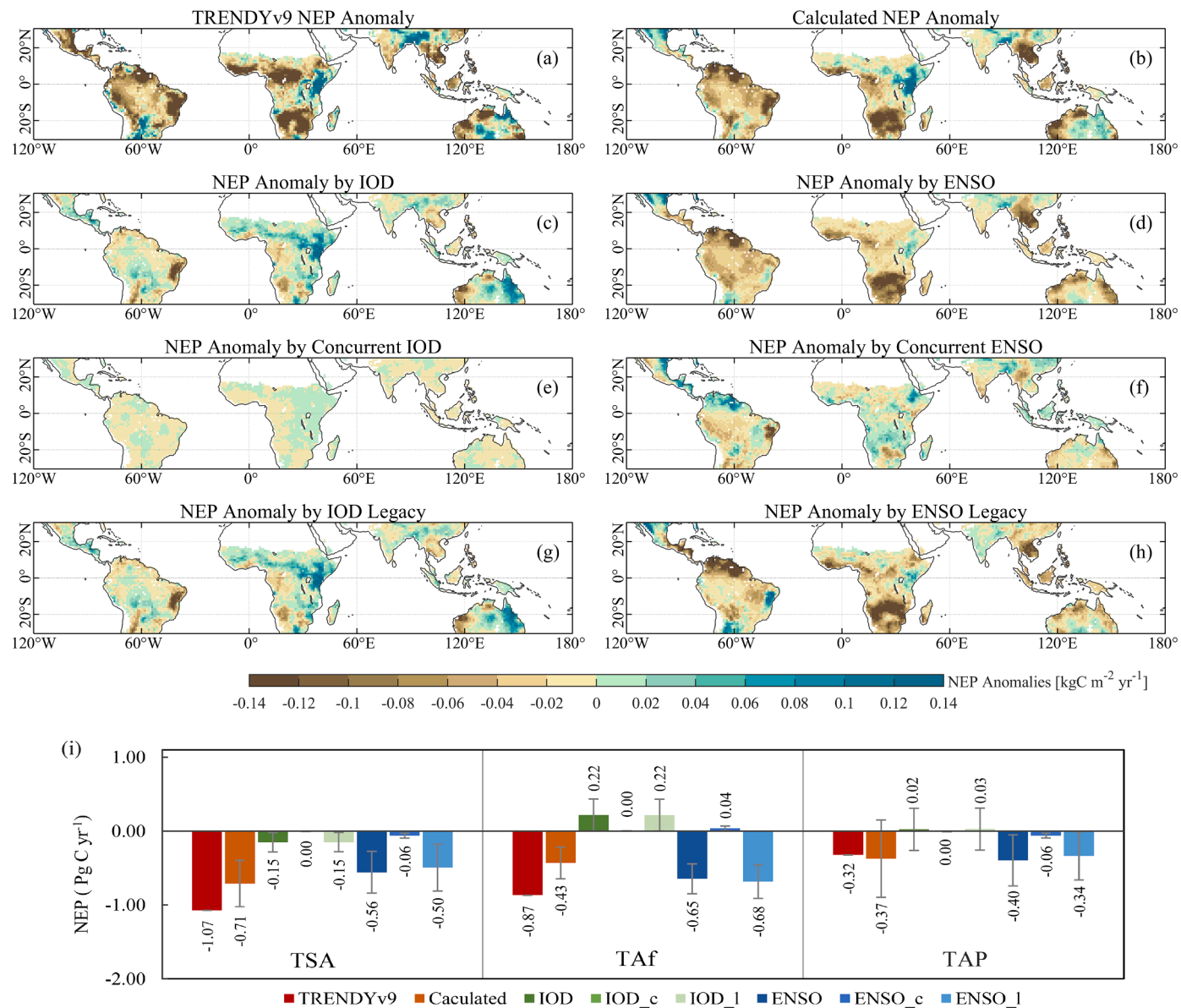


Fig. 9. Same as Fig. 7, but for MAM in 1998.

Declaration of Competing Interest

The authors declare no competing interests.

Data availability

Land precipitation and surface air temperature from CRU TS v. 4.05 are available at <https://catalogue.ceda.ac.uk/uuid/c26a65020a5e4b80b20018f148556681>. Sea surface temperature dataset from ERSSTv5 is available at <https://psl.noaa.gov/data/gridded/data.noaa.ersst.v5.html>. The TRENDY DGVMs data are available at <https://sites.exeter.ac.uk/trendy>.

Acknowledgments

We gratefully acknowledge the TRENDY DGVM community, as part of the Global Carbon Project, for access to gridded land data. The calculations in this paper have been done on the computing facilities in the High Performance Computing Center (HPCC) of Nanjing University.

This study was supported by the National Key Research and Development Program of China (grant no. 2021YFB3901001), the Natural Science Foundation of Jiangsu Province, China (BK20221449), the National Natural Science Foundation of China (42030509), the Research Funds for the Frontiers Science Center for Critical Earth Material Cycling, Nanjing University (0904-14380031), and the open project of Key Laboratory of Meteorological Disaster (KLME), Ministry of Education & Collaborative Innovation Center on Forecast and Evaluation of Meteorological Disasters (CIC-FEMD), Nanjing University of Information Science & Technology (grant no. KLME202203).

Supplementary materials

Supplementary material associated with this article can be found, in the online version, at [doi:10.1016/j.agrformet.2023.109472](https://doi.org/10.1016/j.agrformet.2023.109472).

References

Ashok, K., Guan, Z.Y., Saji, N.H., Yamagata, T., 2004. Individual and combined influences of ENSO and the Indian Ocean Dipole on the Indian summer monsoon. *J. Clim.* 17 (16), 3141–3155.

Bacastow, R.B., 1976. Modulation of atmospheric carbon dioxide by the Southern Oscillation. *Nature* 261, 116–118.

Bastos, A., et al., 2018. Impact of the 2015/2016 El Niño on the terrestrial carbon cycle constrained by bottom-up and top-down approaches. *Philos. Trans. R. Soc. Lond. B Biol. Sci.* 373 (1760).

Bastos, A., et al., 2016. European land CO₂ sink influenced by NAO and East-Atlantic Pattern coupling. *Nat. Commun.* 7, 10315.

Bousquet, P., et al., 2000. Regional changes in carbon dioxide fluxes of land and oceans since 1980. *Science* 290 (5495), 1342–1346.

Bowman, D.M.J.S., et al., 2009. Fire in the Earth System. *Science* 324 (5926), 481–484.

Bowman, K.W., et al., 2017. Global and Brazilian Carbon Response to El Niño Modoki 2011–2010. *Earth. Space Sci.* 4 (10), 637–660.

Cai, W., et al., 2014a. Increasing frequency of extreme El Niño events due to greenhouse warming. *Nat. Clim. Chang* 4 (2), 111–116.

Cai, W., Cowan, T., Raupach, M., 2009. Positive Indian Ocean Dipole events precondition southeast Australia bushfires. *Geophys. Res. Lett.* 36 (19).

Cai, W., et al., 2014b. Increased frequency of extreme Indian Ocean Dipole events due to greenhouse warming. *Nature* 510 (7504), 254–258.

Cai, W., van Renssch, P., Cowan, T., Hendon, H.H., 2011. Teleconnection Pathways of ENSO and the IOD and the Mechanisms for Impacts on Australian Rainfall. *J. Clim.* 24 (15), 3910–3923.

Delire, C., et al., 2020. The global land carbon cycle simulated with ISBA-CTRP: improvements over the last decade. *J. Adv. Model. Earth Syst.* 12 (9).

Fang, Y., et al., 2017. Global land carbon sink response to temperature and precipitation varies with ENSO phase. *Environ. Res. Lett.* 12 (6).

Friedlingstein, P., et al., 2020. Global carbon budget 2020. *Earth Syst. Sci. Data* 12 (4), 3269–3340.

Goll, D.S., et al., 2017. A representation of the phosphorus cycle for ORCHIDEE (revision 4520). *Geosci. Model Dev.* 10 (10), 3745–3770.

Ham, Y.-G., Choi, J.-Y., Kug, J.-S., 2016. The weakening of the ENSO–Indian Ocean Dipole (IOD) coupling strength in recent decades. *Clim. Dyn.* 49 (1–2), 249–261.

Hameed, S.N., Jin, D., Thilakan, V., 2018. A model for super El Niño. *Nat. Commun.* 9 (1), 2528.

Harris, I., Osborn, T.J., Jones, P., Lister, D., 2020. Version 4 of the CRU TS monthly high-resolution gridded multivariate climate dataset. *Sci. Data* 7 (1), 109.

He, B., et al., 2022. Worldwide impacts of atmospheric vapor pressure deficit on the interannual variability of terrestrial carbon sinks. *Natl. Sci. Rev.* 9 (4), nwab150.

Huang, B., et al., 2017. Extended reconstructed sea surface temperature, version 5 (ERSSTv5): upgrades, validations, and intercomparisons. *J. Clim.* 30 (20), 8179–8205.

Humphrey, V., et al., 2021. Soil moisture–atmosphere feedback dominates land carbon uptake variability. *Nature* 592 (7852), 65–69.

Humphrey, V., et al., 2018. Sensitivity of atmospheric CO₂ growth rate to observed changes in terrestrial water storage. *Nature* 560, 628–631.

Jain, A.K., Meiyappan, P., Song, Y., House, J.I.I., 2013. CO₂ emissions from land-use change affected more by nitrogen cycle, than by the choice of land-cover data. *Glob. Chang Biol.* 19 (9), 2893–2906.

Jones, P.W., 1999. First- and second-order conservative remapping schemes for grids in spherical coordinates. *Mon. Weather Rev.* 127 (9), 2204–2210.

Jung, M., et al., 2017. Compensatory water effects link yearly global land CO₂ sink changes to temperature. *Nature* 541 (7638), 516–520.

Kao, H.-Y., Yu, J.-Y., 2009. Contrasting Eastern-Pacific and Central-Pacific Types of ENSO. *J. Clim.* 22 (3), 615–632.

Kim, J.-S., Jeong, S.-J., Kug, J.-S., Williams, M., 2019. Role of local air-sea interaction in fire activity over equatorial Asia. *Geophys. Res. Lett.* 46 (24), 14789–14797.

Kim, J.S., Kug, J.S., Jeong, S.J., 2017. Intensification of terrestrial carbon cycle related to El Niño–Southern Oscillation under greenhouse warming. *Nat. Commun.* 8.

Krinner, G., et al., 2005. A dynamic global vegetation model for studies of the coupled atmosphere–biosphere system. *Global Biogeochem. Cycles* 19 (1).

Lienert, S., Joos, F., 2018. A Bayesian ensemble data assimilation to constrain model parameters and land-use carbon emissions. *Biogeosciences* 15 (9), 2909–2930.

Liu, J., et al., 2017. Contrasting carbon cycle responses of the tropical continents to the 2015–2016 El Niño. *Science* 358 (6360).

Luo, X., et al., 2018. The impact of the 2015/2016 El Niño on global photosynthesis using satellite remote sensing. *Philos. Trans. R. Soc. Lond. Ser. B Biol. Sci.* 373 (1760).

Melton, J.R., et al., 2020. CLASSIC v1.0: the open-source community successor to the Canadian Land Surface Scheme (CLASS) and the Canadian Terrestrial Ecosystem Model (CTEM) – Part 1: model framework and site-level performance. *Geosci. Model Dev.* 13 (6), 2825–2850.

Mercado, L.M., et al., 2009. Impact of changes in diffuse radiation on the global land carbon sink. *Nature* 458 (7241), 1014–1087.

Peylin, P., et al., 2013. Global atmospheric carbon budget: results from an ensemble of atmospheric CO₂ inversions. *Biogeosciences* 10 (10), 6699–6720.

Phillips, O.L., et al., 2009. Drought sensitivity of the Amazon Rainforest. *Science* 323 (5919), 1344–1347.

Piao, S., et al., 2019. Interannual variations of terrestrial carbon cycle: issues and perspectives. *Glob. Chang Biol.*

Piao, S.L., et al., 2020. Interannual variation of terrestrial carbon cycle: issues and perspectives. *Glob. Chang Biol.* 26 (1), 300–318.

Poulter, B., Frank, D.C., Hodson, E.L.L., Zimmermann, N.E., 2011. Impacts of land cover and climate data selection on understanding terrestrial carbon dynamics and the CO₂ airborne fraction. *Biogeosciences* 8 (8), 2027–2036.

Preethi, B., Sabin, T.P., Adedoyin, J.A., Ashok, K., 2015. Impacts of the ENSO Modoki and other tropical Indo-Pacific climate-drivers on African Rainfall. *Sci. Rep.* 5 (1), 16653.

Rogers, A., 2014. The use and misuse of Vc,max in Earth system models. *Photosynth Res.* 119 (1–2), 15–29.

Rogers, A., et al., 2017. A roadmap for improving the representation of photosynthesis in Earth system models. *New Phytol.* 213 (1), 22–42.

Saji, N.H., Goswami, B.N., Vinayachandran, P.N., Yamagata, T., 1999. A dipole mode in the tropical Indian Ocean. *Nature* 401 (6751), 360–363.

Saji, N.H., Yamagata, T., 2003. Possible impacts of Indian Ocean Dipole mode events on global climate. *Clim. Res.* 25 (2), 151–169.

Sitch, S., et al., 2015. Recent trends and drivers of regional sources and sinks of carbon dioxide. *Biogeosciences* 12 (3), 653–679.

Tian, H., et al., 2015. North American terrestrial CO₂ uptake largely offset by CH₄ and N₂O emissions: toward a full accounting of the greenhouse gas budget. *Clim. Change* 129 (3), 413–426.

Trenberth, K.E., Caron, J.M., Stepaniak, D.P., Worley, S., 2002. Evolution of El Niño–Southern Oscillation and global atmospheric surface temperatures. *J. Geophys. Res. Atmospheres* 107 (D8). AAC 5-1–AAC 5-17.

Trenberth, K.E., et al., 2007. Observations: surface and atmospheric climate change. In: Solomon, S., et al. (Eds.), *Climate Change 2007: The Physical Science Basis. Contribution of Working Group I to the Fourth Assessment Report of the Intergovernmental Panel On Climate Change*. Cambridge University Press, Cambridge, United KingdomNew York, NY, USA.

van der Velde, I.R., et al., 2021. Vast CO₂ release from Australian fires in 2019–2020 constrained by satellite. *Nature* 597 (7876), 366–369.

van der Werf, G.R., et al., 2004. Continental-scale partitioning of fire emissions during the 1997 to 2001 El Niño/La Niña period. *Science* 303 (5654), 73–76.

Vuichard, N., et al., 2019. Accounting for carbon and nitrogen interactions in the global terrestrial ecosystem model ORCHIDEE (trunk version, rev 4999): multi-scale evaluation of gross primary production. *Geosci. Model Dev.* 12 (11), 4751–4779.

Walker, A.P., et al., 2017. The impact of alternative trait-scaling hypotheses for the maximum photosynthetic carboxylation rate (V_{cmax}) on global gross primary production. *New Phytol.* 215 (4), 1370–1386.

Wang, J., et al., 2020. Spaceborne detection of CO₂ enhancement induced by Australian mega-bushfires. *Environ. Res. Lett.* 15 (12).

Wang, J., et al., 2021. Modulation of land photosynthesis by the Indian Ocean Dipole: satellite-based observations and CMIP6 future projections. *Earth's Future* 9 (4).

Wang, J., Zeng, N., Wang, M., 2016. Interannual variability of the atmospheric CO₂ growth rate: roles of precipitation and temperature. *Biogeosciences* 13 (8), 2339–2352.

Wang, J., et al., 2018a. Contrasting interannual atmospheric CO₂ variabilities and their terrestrial mechanisms for two types of El Niño. *Atmos. Chem. Phys.* 18 (14), 10333–10345.

Wang, J., et al., 2018b. Contrasting terrestrial carbon cycle responses to the 1997/98 and 2015/16 extreme El Niño events. *Earth Syst. Dyn.* 9 (1), 1–14.

Wang, W., et al., 2013. Variations in atmospheric CO₂ growth rates coupled with tropical temperature. *PNAS* 110, 13061–13066.

Williams, C.A., Hanan, N.P., 2011. ENSO and IOD teleconnections for African ecosystems: evidence of destructive interference between climate oscillations. *Biogeosciences* 8 (1), 27–40.

Yang, J., et al., 2018. Amazon drought and forest response: largely reduced forest photosynthesis but slightly increased canopy greenness during the extreme drought of 2015/2016. *Glob. Chang. Biol.* 24 (5), 1919–1934.

Yang, Y., et al., 2015. Seasonality and predictability of the Indian Ocean dipole mode: ENSO forcing and internal variability. *J. Clim.* 28 (20), 8021–8036.

Zaehle, S., et al., 2010. Carbon and nitrogen cycle dynamics in the O-CN land surface model: 2. Role of the nitrogen cycle in the historical terrestrial carbon balance. *Global Biogeochem. Cycles* 24 (1).

Zeng, N., Mariotti, A., Wetzel, P., 2005. Terrestrial mechanisms of interannual CO₂ variability. *Global Biogeochem. Cycles* 19 (1).